Available online at www.sciencedirect.com
ScienceDirect
International Journal of Heat and Mass Transfer 51 (2008) 2637–2650
International Journal of HEAT and MASS TRANSFER
www.elsevier.com/locate/ijhmt

Unsteady natural convection in a water-filled isosceles triangular enclosure heated from below

Chengwang Lei [a,*], Steven W. Armfield [b], John C. Patterson [a]

[a] School of Engineering, James Cook University, Townsville, QLD. 4811, Australia
[b] School of Aerospace, Mechanical and Mechatronic Engineering, The University of Sydney, Sydney, NSW 2006, Australia

Received 21 May 2007; received in revised form 27 September 2007
Available online 3 December 2007

Abstract

This study is concerned with transient natural convection in a water-filled isosceles triangular enclosure subject to cooling at the inclined surfaces and simultaneous heating at the base. The unsteady flows over a range of Grashof numbers are visualized using a shadowgraph technique, and corresponding numerical simulations are carried out using a Finite Volume Method. Both the experiments and numerical simulations have revealed that the transient flow development in the enclosure due to abrupt heating and cooling through the boundaries can be classified into three distinct stages, that is, an early stage, a transitional stage, and a steady/quasi-steady stage. The major flow features at each of the three stages are described and the Grashof number effects on the flow development and heat transfer are discussed. It is found that, for a fixed aspect ratio of 0.5, a transition of the unsteady flow from symmetric to asymmetric structures occurs for Grashof numbers above 2.95×10^4. Moreover, the present heat transfer calculations indicate that the average Nusselt number over the inclined and horizontal surfaces approximately scales with $Gr^{0.2}$.

Keywords: Natural convection; Triangular enclosure; Pitchfork bifurcation; Shadowgraph visualization

1. Introduction

Natural convection in triangular enclosures finds applications in many domestic and industrial systems as well as in geophysical flows. One application which has attracted a great deal of attention is heat transfer by natural convection through attics of buildings. The geometry of the attics of domestic and industrial buildings often has an isosceles triangular cross-section with two inclined surfaces (the roof) and a horizontal surface (the ceiling or base). In field situations, the temperature on the roof varies with the outside conditions, whereas the temperature on the ceiling depends on the inside conditions. In typical diurnal cycles, heating by solar radiation in the daytime results in a higher temperature on the roof than that on the base; cooling by atmospheric air at the night-time results in a lower temperature on the roof; and the daytime heating and night-time cooling apply alternatively over diurnal cycles. The temperature differences between the roof and ceiling produces a spatial distribution of the air density within the attics, which in turn initiates heat transfer by natural convection.

Owing to the significance of attics for the thermal comfort of occupants in buildings and the ensuing energy costs for heating and air-conditioning, over the last three decades increasing research activities have been devoted to topics relevant to heat transfer in attics. Most of the previous research has focused on the fundamental fluid dynamics in attics induced by natural convection [1–4], which is also the focus of this paper. Studies of natural convection in attics first appeared in the literature in the 1970s [5] and were continued in the 1980s through the 1990s [6–8]. In recent years, there have been increasing research activities in this area [9–16].

A survey of the literature reveals that the majority of the existing literature is concerned with steady-state flows and

* Corresponding author. Tel.: +61 7 4781 4172; fax: +61 7 4781 6788.
E-mail address: Chengwang.Lei@jcu.edu.au (C. Lei).

0017-9310/$ - see front matter © 2007 Elsevier Ltd. All rights reserved.
doi:10.1016/j.ijheatmasstransfer.2007.09.036

Nomenclature

A	aspect ratio
B	half length of the base
g	acceleration due to gravity
Gr	Grashof number
Gr_c	critical Grashof number
H	height of the enclosure
$\bar{h}$	average heat transfer coefficient
k	thermal conductivity
$\overline{Nu}$	average Nusselt number
$\lvert\overline{Nu}\rvert_{base}$	average Nusselt number on the base
$\lvert\overline{Nu}\rvert_{roof}$	average Nusselt number on the roof
p	pressure
Pr	Prandtl number
q''	local heat flux
$\bar{q}''$	average heat flux over a surface
Ra	Rayleigh number
t_c	critical time for transition
t_s	flow development time
T	temperature
T_H	temperature at the base
T_L	temperature on the roof
T_0	initial fluid temperature
u, v	velocity components in x- and y-directions
x, y	horizontal and vertical coordinates

Greek symbols

α	thermal diffusivity
β	coefficient of thermal expansion
ΔT	temperature difference
ν	kinematic viscosity
ρ	density

heat transfer [7,11,17], and only a few studies have considered the transient flow response in attics [2,4,8,18,19]. Among these investigations, Poulikakos and Bejan [2] adopted a scaling procedure to describe the transient flow development; Karyakin et al. [18] and Salmun [8] numerically simulated the transient flow response to different thermal forcing conditions; Ridouane and Campo [4] numerically observed the formation of a pitchfork bifurcation, which results in asymmetric flow structures in an isosceles triangular enclosure; and Lei et al. [19] is the only reported experiment targeting the unsteady features of the natural convection flow during a transition to a steady state.

Existing studies have considered mainly two types of thermal forcing conditions for attics: the daytime condition and the night-time condition. For both conditions, a pioneering experiment was carried out by Flack [17] who visualized the flow structures and measured the heat transfer. He found that the flow remained stable and laminar for the daytime condition. However, the flow underwent a transition from laminar to turbulent as the Grashof number was increased under the night-time condition.

The night-time attic problem was reinvestigated experimentally by Poulikakos and Bejan [1] for Rayleigh numbers relevant to field situations. Their flow visualization indicated a turbulent flow in the attic, consistent with the observations of Flack [17]. The same problem was again investigated analytically and numerically by Poulikakos and Bejan [2], who obtained an asymptotic solution of the steady state flow with a single circulation cell in a right-angled triangle (half of the domain) for small aspect ratios.

The single-cell steady-state solution of the night-time flow reported in [2] was later questioned by Salmun [8], who carried out two-dimensional (2D) numerical simulations for a range of aspect ratios and Rayleigh numbers. It was reported in [8] that the single-cell flow structure existed only for a certain range of the parameter domain. As the Rayleigh number was increased beyond a certain value, a bifurcation took place, and a multi-cellular steady-state solution was expected. The later numerical simulations of [3,10] have both given support to the argument of Salmun [8]. Asan and Namli [10] examined the details of the transition from a single-cell to multi-cell flow structures, and revealed that both the aspect ratio and Rayleigh number had a profound influence on the flow field. Haese and Teubner [20] also confirmed the dependence of the flow transition from a single-cell to multi-cellular structures on the aspect ratio and Rayleigh number.

An interesting issue regarding the symmetry of the flow with respect to the geometric symmetry plane of attics subject to night-time cooling arose from the previous investigations. Although a full isosceles triangular domain was adopted in some early studies [7,18], a number of investigations [1,2,6,8,20] have adopted a right-angled triangle with an adiabatic vertical wall, which effectively constituted only half of the full domain. A presumption of the half-domain model was that the flow in the attic was symmetric about the geometric mid-plane.

However, Holtzman et al. [3] revealed that the natural convection flow in an isosceles triangular domain undergoes a transition from symmetric to asymmetric structures. For low Grashof numbers, their numerical solutions show symmetric structures about the geometric plane of symmetry with single-cell structures on both sides of the mid-plane. As the Grashof number increases above a critical value, the symmetric solutions become unstable, and asymmetric solutions are obtained. The critical Grashof number Gr_c is found to be dependent on the aspect ratio A (e.g. $Gr_c = 5360$ for $A = 0.2$, 8930 for $A = 0.5$, and 16,200 for $A = 1.0$). Holtzman et al. [3] also conducted a simple flow visualization experiment by slowly injecting smoke into

the enclosure, and the observed flow patterns supported their numerical solutions. The reported transition from symmetric to asymmetric flows with increasing Grashof numbers was confirmed by a recent numerical calculation of Ridouane and Campo [4]. However, these results clearly contradict many other reported works, and thus are yet to be further investigated. This has motivated the present investigation.

In this study, flow visualization using a shadowgraph technique is carried out to observe the transient flow development in an isosceles triangular enclosure subject to constant cooling from the inclined surfaces and simultaneous heating at the base. Corresponding numerical simulations are also conducted to examine further details of the flow and heat transfer in the attic model. It is worth noting that, in order to facilitate the flow visualization with the shadowgraph technique, we adopted water instead of air as the medium in the attics model. Therefore, care must be taken when applying the present results to air-filled attic problems.

In the rest of this paper, Section 2 provides details of the experimental procedures; Section 3 provides details of the numerical simulations; Section 4 presents the results from both the experiments and simulations; and Section 5 summarizes major findings from this investigation.

2. Details of the experimental system and approach

Fig. 1a shows a schematic of the experimental model. The shaded section in Fig. 1a represents a water-filled isosceles triangular enclosure, which has a height of $H = 24$ mm, a base length of $2B = 96$ mm, and a width of 48 mm in the lateral direction. These dimensions were initially chosen so that the range of the parameters examined in [3], which covered the critical condition for the transition from symmetric to asymmetric flows, can be achieved in the laboratory experiments with this model. Due to the difficulties in the shadowgraph flow visualization with air, the experiments reported here were conducted with water as the medium. The base and inclined surfaces of the attic model are made of aluminum plates of 1-mm thickness, and a thermal insulation layer is inserted between the inclined surfaces and the base to avoid direct contact between them. The two end surfaces in the direction normal to the page are made of 10-mm thick transparent Perspex sheets to allow shadowgraph flow visualization. The inclined surfaces and the base of the attic model form parts of two separate water tanks, one upper tank for cooling and the other lower tank for heating. The rest of the surfaces of both the heating and cooling water tanks are also made of transparent Perspex sheets of 10-mm thickness.

Before the start of each experiment, proper procedures are followed in order to achieve an initially isothermal (with a temperature T_0) and stationary medium in the triangular enclosure. At the start of the experiment, cold and hot waters of constant temperatures T_L ($T_L < T_0$) and T_H ($T_H > T_0$), respectively, are circulated through the upper and lower water tanks to cool the inclined surfaces and simultaneously heat the base. The temperatures of the circulating waters are controlled by two independent Julabo refrigerated and heating circulators, which maintain a temperature stability of ± 0.01 °C. The time it takes to fill the upper and lower tanks and thus establish uniform and constant cooling and heating at the surfaces is only a fraction of one second, which is very small compared with a boundary layer startup time (refer to Section 4). Therefore, a sudden startup of heating and cooling may be assumed.

Following the startup of the thermal forcing on the boundaries, heat is then transferred from the bottom tank through the attic model to the top tank by combined conduction and convection processes. The rate of heat transfer through the model depends on the flow and temperature

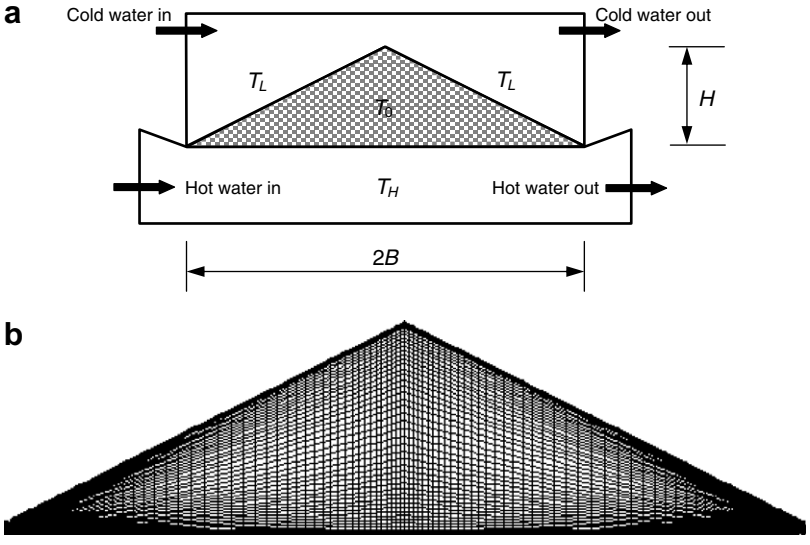

Fig. 1. (a) Schematic of the experimental model. (b) A sample mesh showing the major features of the non-uniform symmetric meshes adopted in this study.

structures inside the enclosure, which are governed by the following three dimensionless parameters:

$$\text{Aspect ratio}: A = \frac{H}{B}, \tag{1}$$

$$\text{Prandtl number}: Pr = \frac{v}{\alpha}, \tag{2}$$

$$\text{Grashof number}: Gr = \frac{g\beta\Delta T H^3}{v^2}. \tag{3}$$

All the fluid properties are evaluated at the reference temperature T_0. In practice, it is common to combine the Prandtl and Grashof numbers to form a Rayleigh number (Ra) as follows:

$$Ra = Pr \cdot Gr. \tag{4}$$

In this study, the aspect ratio of the attic model is fixed at $A = 0.5$, and the reference (initial) temperature of the water is fixed at $T_0 = 20.5$ °C, which is determined by the air-conditioned room temperature. Therefore, the Prandtl number of the water is fixed at $Pr \approx 7$. The Grashof number is controlled by varying the temperatures T_H and T_L of the circulating waters. Five sets of experiments with different Grashof numbers are conducted in this study. The experimental parameters are listed in Table 1.

The temperature and flow structures in the isosceles triangular enclosure are visualized using a shadowgraph technique. The principle of the shadowgraph technique [21,22] is to pass an originally parallel light beam through a field of interest and observe the deflection of the beam caused by the temperature gradient in the flow field. The deflected light pattern, observed after exiting the flow field, is known as a shadowgraph, and may be roughly interpreted as representing the second spatial derivative of the temperature field. A time series of shadowgraph images is a representation of the temporal evolution of the temperature field. The shadowgraph technique provides a very simple, extremely sensitive and totally non-intrusive tool for visualizing the temperature field of fluid flows involving thermal gradients, and has been extensively used to visualize buoyancy-driven flows in rectangular and other irregularly shaped cavities [23–27].

The basic optical set-up used for the present shadowgraph visualization is the same as that described in [26,27]. In brief, a point white light source is placed at the focal point of a spherical mirror, which collimates the lights from the point light source to form a parallel light beam. The parallel light beam is then passed through the flow field of interest, and is recollected by another identical spherical mirror after exiting the flow field. The second spherical mirror also refocuses the collected light patterns onto the focal point of a CCD camera, which is connected to a personal computer for recording the images.

Table 1
Experimental parameters for shadowgraph flow visualization ($A = 0.5$)

No.	T_0 (°C)	T_H (°C)	T_L (°C)	ΔT (°C)	Pr	Gr
1	20.5	22.5	18.5	4	7.06	1.18×10^5
2		23.5	17.5	6		1.77×10^5
3		24.5	16.5	8		2.36×10^5
4		25.5	15.5	10		2.95×10^5
5		28.5	12.5	16		4.73×10^5

3. Details of the numerical procedures and tests

Two-dimensional numerical simulations corresponding to the experiments described previously have been carried out in this study. For this purpose, an isosceles triangular domain with dimensions the same as those of the experimental model is considered, and a Cartesian coordinate system is adopted with the origin located at the center of the base, the x-direction pointing horizontally, and the y-direction pointing vertically. The initial and boundary conditions for the numerical simulations are also specified in accordance with the experiments. That is, the water in the enclosure is initially motionless and isothermal with a uniform temperature of T_0. At the time $t = 0$, the two inclined surfaces and the base of the enclosure are subject to instantaneous cooling and heating at constant temperatures T_L and T_H, respectively. All the interior surfaces of the enclosure are assumed rigid and no slip.

The evolution of the temperature and flow fields in the triangular enclosure following the start-up, which is dominated by natural convection, may be described by the following set of governing equations, for which the Boussinesq assumption has been made:

$$\frac{\partial u}{\partial x} + \frac{\partial v}{\partial y} = 0, \tag{5}$$

$$\frac{\partial u}{\partial t} + u\frac{\partial u}{\partial x} + v\frac{\partial u}{\partial y} = -\frac{1}{\rho}\frac{\partial p}{\partial x} + v\left(\frac{\partial^2 u}{\partial x^2} + \frac{\partial^2 u}{\partial y^2}\right), \tag{6}$$

$$\frac{\partial v}{\partial t} + u\frac{\partial v}{\partial x} + v\frac{\partial v}{\partial y} = -\frac{1}{\rho}\frac{\partial p}{\partial y} + v\left(\frac{\partial^2 v}{\partial x^2} + \frac{\partial^2 v}{\partial y^2}\right) + g\beta(T - T_0), \tag{7}$$

$$\frac{\partial T}{\partial t} + u\frac{\partial T}{\partial x} + v\frac{\partial T}{\partial y} = \alpha\left(\frac{\partial^2 T}{\partial x^2} + \frac{\partial^2 T}{\partial y^2}\right). \tag{8}$$

The above governing equations along with the specified initial and boundary conditions are solved using a finite volume method. The SIMPLE scheme [28] is adopted for pressure–velocity coupling; the spatial discretization is done by a second-order upwind scheme; and the time marching is carried out by a second-order implicit scheme. In order to avoid the singularities at the intersection points between the roofs and the base, the tips on both sides of the geometric symmetry plane are cut by approximately 4% relative to the half length of the base, and vertical adiabatic and rigid walls are added at the cutting points (refer to Fig. 1b). It is anticipated that this slight modification of the flow domain does not have a significant impact on the calculated flow and heat transfer features.

In the numerical simulations, the aspect ratio of the enclosure is also fixed at 0.5. Seven sets of flow parameters (see Table 2) are calculated in order to examine the transition of the flow from symmetric to asymmetric structures.

Table 2
Flow parameters for the numerical simulations ($A = 0.5$)

No.	T_0 (°C)	T_H (°C)	T_L (°C)	ΔT (°C)	Pr	Gr
1	20.5	20.6	20.4	0.2	7.06	5.91×10^3
2		20.75	20.25	0.5		1.48×10^4
3		21	20	1		2.95×10^4
4		21.5	19.5	2		5.91×10^4
5		22.5	18.5	4		1.18×10^5
6		24.5	16.5	8		2.36×10^5
7		28.5	12.5	16		4.73×10^5

Note that the numerical cases 5, 6 and 7 listed in Table 2 correspond to the experimental cases 1, 3 and 5, respectively, listed in Table 1.

For the discretization of the flow domain, non-uniform and symmetric meshes are constructed within the flow domain with nodes clustered toward all interior surfaces and the geometric symmetry plane. A sample mesh is given in Fig. 1b, showing the major features of the numerical meshes. Before the calculations are carried out for different Grashof numbers, mesh and time-step dependence tests are conducted for the highest Grashof number case, i.e. $Gr = 4.73 \times 10^5$. Three different meshes (see Table 3) with the total numbers of finite-volume cells of 4000, 16,000 and 64,000, respectively, are tested. The time steps adopted for the coarse, medium and fine meshes are 0.1, 0.05 and 0.025 s, respectively, so that the CFL (Courant–Freidrich–Lewy) numbers remain the same for the mesh and time-step dependence tests. The results obtained with the three meshes are compared in Table 3, which presents the time-averaged temperature at a location above the base and on the geometric symmetry plane and the time-averaged surface heat flux over the base at quasi-steady states (refer to Section 4 for more details). The variations shown in Table 3 are calculated with reference to the quantities obtained with the finest mesh. It is seen that the variation of the numerical results between the medium and fine meshes is very small. Therefore, the medium mesh with 16,000 cells and a time step of 0.05 s are adopted for the present simulations.

4. Results and discussion

In this section, the transient development of the flow in the isosceles triangular enclosure in response to the abrupt heating and cooling through the horizontal and inclined boundaries is described based on the shadowgraph flow visualization and numerical simulations. Other features of the transient flow and heat transfer, as well as their dependence on the Grashof number, are further explored based on numerical data.

4.1. Transient flow development at $Gr = 2.36 \times 10^5$

Here, the overall features of the flow development in the isosceles triangular enclosure are described based on the case with a temperature difference $\Delta T = 8$ °C, corresponding to a Grashof number of $Gr = 2.36 \times 10^5$. The transient flow development at this Grashof number can be roughly classified into three stages: an early stage, a transitional stage and a quasi-steady stage. Each of the three stages of the flow development is described below.

4.1.1. Early stage flow

As mentioned previously, the water in the isosceles triangular enclosure is initially isothermal and stationary. At the startup of the experiment and the numerical simulation, instantaneous isothermal conditions are established over all the surfaces, which cool the enclosure through the inclined surfaces and heat the enclosure through the base. As a consequence, thermal boundary layers develop along all the interior surfaces. Among them, the thermal boundary layer adjacent to the base is a heating thermal boundary layer, and those adjacent to the inclined surfaces are cooling thermal boundary layers. The growth of these thermal boundary layers with time can be observed in Fig. 2, which shows the experimental shadowgraph images and corresponding numerical isotherms and contours of stream functions at two time instances following the startup. The elapsed time measured in seconds from the startup is displayed on the upper-left corner of each plot.

It is seen from the numerical isotherms in Fig. 2 that, despite the growth of the thermal boundary layers inside the enclosure, the water in the core remains isothermal at the initial temperature (20.5 °C) at the early stage. The comparison between the isotherms at the two different times clearly indicates the increase with time of the thicknesses of all three thermal boundary layers toward the core. The contours of the stream functions at this stage show two weak counter-rotating cells, one on each side of the geometric symmetry plane, which are formed due to entrainment of the cooling thermal boundary layers. The numerical flow is apparently symmetric at this stage.

The observed shadowgraphs basically show the same features as the numerical flow. However, the heating and cooling thermal boundary layers appear differently in the

Table 3
Mesh and time-step dependence tests for $Gr = 4.73 \times 10^5$

No.	Mesh size	Number of cells	Time step (s)	Temperature		Heat flux	
				°C	Variation (%)	W/m^2	Variation (%)
1	100×40	4000	0.1	23.65	2.8	4950	2.9
2	200×80	16,000	0.05	23.02	0.04	5067	0.6
3	400×160	64,000	0.025	23.01	–	5097	–

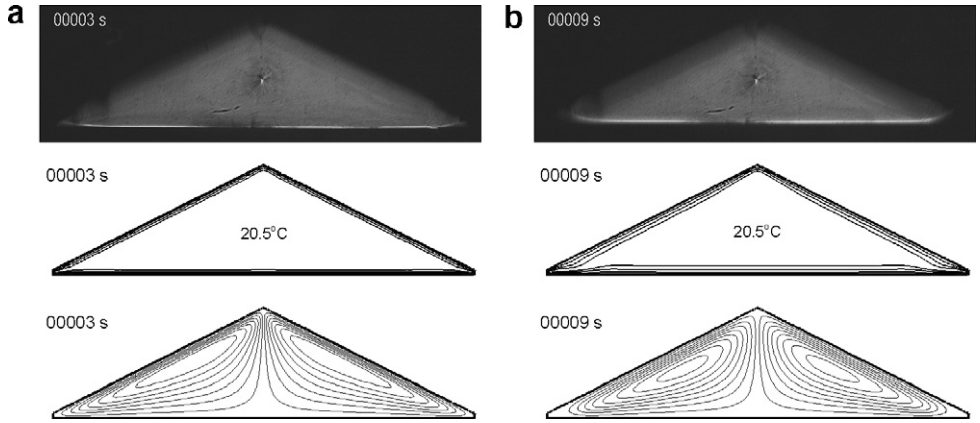

Fig. 2. Growth of thermal boundary layers in the early stage ($Gr = 2.36 \times 10^5$). From top to bottom: shadowgraph images, isotherms with 1 °C interval, and contours of stream functions with intervals of (a) 1.5×10^{-4} and (b) 6.0×10^{-4} m^2/s.

shadowgraph images. This is caused by the different temperature profiles in the heating and cooling thermal boundary layers, which results in different refraction indices of the water. In the heating thermal boundary layer above the base, the originally parallel light is deflected in a way that it concentrates onto a line so that a horizontal bright band is formed above the base (see Fig. 2). This bright band approximately represents the upper edge of the thermal boundary layer above the base, and it moves upwards as the heating continues, indicating the growth of the thermal boundary layer toward the core. Therefore, the thickness of the heating thermal boundary layer may be estimated according to the position of this bright band [25,26]. In the cooling thermal boundary layers along the inclined surfaces, the light is deflected in a way that it scatters from the thermal boundary layers. Therefore, it is difficult to identify the edges of the cooling thermal boundary layers. However, a growth similar to that of the heating boundary layer is expected for the cooling boundary layers, as has been seen from the numerical isotherms.

It is worth noting that a bright spot is present near the center of the enclosure in the shadowgraph images (see Fig. 2). This bright spot represents a small hole of 1-mm diameter on one of the end surfaces in the page direction, through which water is filled into the enclosure. The center of the hole is on the geometric symmetry plane of the model, and the hole is sealed after the enclosure is filled with water.

Fig. 3 shows subsequent development of the flow in the early stage. While the cooling thermal boundary layers adjacent to the inclined surfaces are growing, the buoyancy effect results in two downward gravity currents, one along each inclined surface. The downward gravity currents change their directions after they reach the bottom tips of the enclosure, and subsequently form two opposing horizontal streams along the base and toward the center of the base. The fronts of the horizontal flows are marked with white arrows in the shadowgraph images shown in Fig. 3. They can also be observed in the numerical isotherms, as indicated by the ramp-like structures near both ends of the heating thermal boundary layer. When the two horizontal streams eventually meet at the center of the base, they form a single ascending stream, which then diverges near the apex of the triangular enclosure. As a consequence, two primary circulation cells are formed, one on each side of the geometric symmetry plane (refer

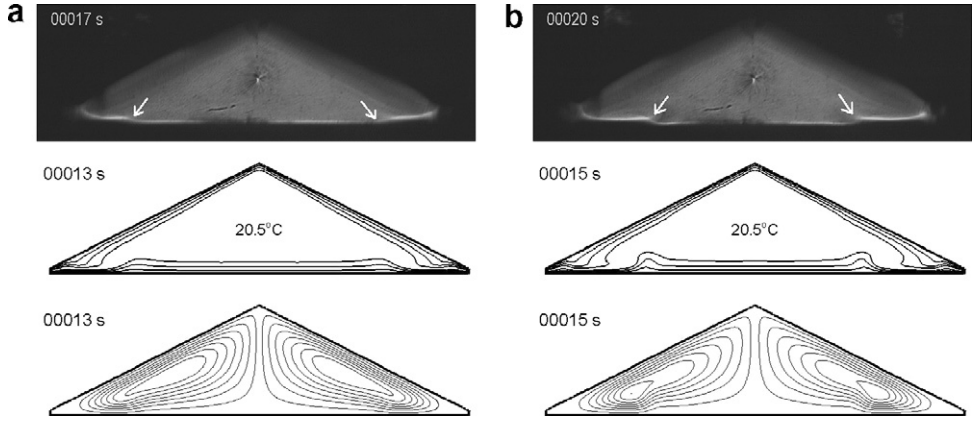

Fig. 3. Formation of convective circulations in the early stage ($Gr = 2.36 \times 10^5$). From top to bottom: shadowgraph images, isotherms with 1 °C interval, and contours of stream functions with intervals of (a) 9.6×10^{-4} and (b) 1.2×10^{-3} m^2/s.

to the contours of the stream functions in Fig. 3). Clearly, both the experimental and numerical flows remain symmetric at this stage.

It is worth noting that the experimental shadowgraph images are compared with the numerical isotherms at different times in Fig. 3. This is because the experimental flow development is slower than the numerical flow development. Similar variations between numerical simulations and experimental observations are reported by Patterson and Armfield [29] in the context of natural convection in a differentially heated square cavity. Patterson and Armfield [29] suggested that the timing difference is a result of achieving a smaller actual Grashof number in the experiment than that in the numerical simulation. Here, the comparisons between the experiments and simulations are based on the flow events rather than the actual flow time.

4.1.2. Transitional stage flow

The transitional stage flow is characterized by the appearance of convective instabilities. On the one hand, heating through the base of the enclosure results in a temperature structure in the horizontal thermal boundary layer with warm water underneath cool water, which is potentially unstable to Rayleigh–Bénard instabilities. When a critical condition is met, the heating thermal boundary layer becomes unstable. In the present case, the instability appears in the form of rising hot-water plumes, as can be seen from the shadowgraph image and the numerical isotherms in Fig. 4a. Due to the existence of the two opposing horizontal flows along the base described previously, the hot-water plumes travel toward the center of the enclosure while they are ascending, resulting in a traveling-wave-like appearance along the horizontal thermal boundary layer.

On the other hand, cooling through the inclined surfaces also results in potentially unstable thermal boundary layers along the surfaces, giving rise to the appearance of sinking cold-water plumes. The instabilities of the cooling thermal boundary layers are initially observed in the two tip regions (Fig. 4a), which are the most unstable regions because of their close proximity to the heated base and the continuous cooling of the fluid along the slope. As the instabilities intensify, they eventually extend to the middle and upper regions of the cooling thermal boundary layers. Due to the occurrence of the convective instabilities, the two-cell flow structures observed at the early stage of the flow development are broken into multiple cells, as shown by the contours of the stream functions in Fig. 4.

The subsequent development of the flow in the enclosure is dominated by the occurrence of convective instabilities. The typical temperature and flow structures observed in the experiment and numerical simulation at the late transitional stage are depicted in Fig. 4b. Here, the experimental and numerical flows at the same time ($t = 50$ s) are compared due to the reduced effects of the time lag between the experiment and simulation at this stage. It is seen from the shadowgraph image in Fig. 4b that the convective instabilities exhibit a certain level of irregularity, and the experimental flow is slightly asymmetric at $t = 50$ s. However, the observation of a number of consecutive shadowgraph images over a certain period of time indicates that the time-averaged flow would remain approximately symmetric at this stage. In contrast to the experimental flow, the numerical flow remains symmetric at this time. The discrepancy between the experimental and numerical flows in terms of the symmetry of the flow is attributed to the presence of stronger perturbations in the experiments compared with those in the numerical simulation.

Despite the above-mentioned discrepancy, both the experimental and numerical flows at $t = 50$ s exhibit two distinct features of the convective instabilities (refer to Fig. 4). First, the wave number of the thermal layer instabilities at $t = 50$ s is apparently larger than that at the earlier time. The subsequent results from both the experiment and simulation show that the wave number remains approximately the same for the rest of the flow development. Second, the thermal layer instabilities become weaker at $t = 50$ s compared with those at the earlier time. The contours of the stream functions at this time show a cellular structure.

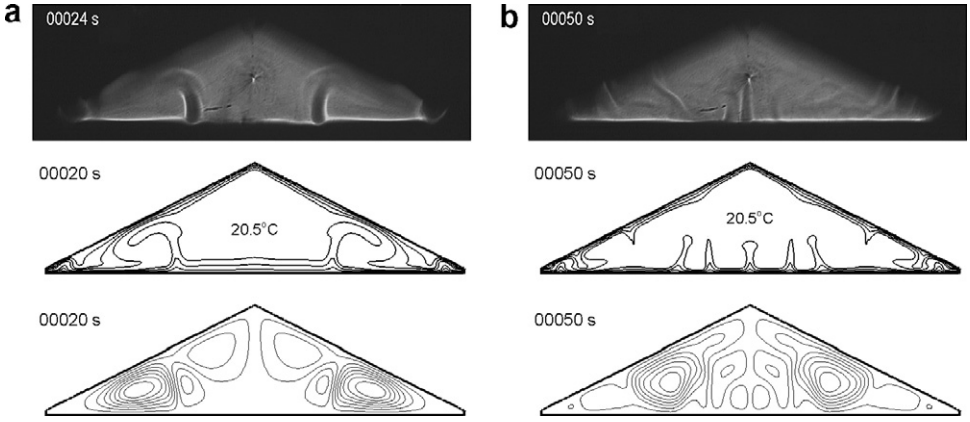

Fig. 4. Transitional stage flow with convective instabilities ($Gr = 2.36 \times 10^5$). From top to bottom: shadowgraph images, isotherms with 1 °C interval, and contours of stream functions with intervals of (a) 1.75×10^{-3} and (b) 1.82×10^{-3} m^2/s.

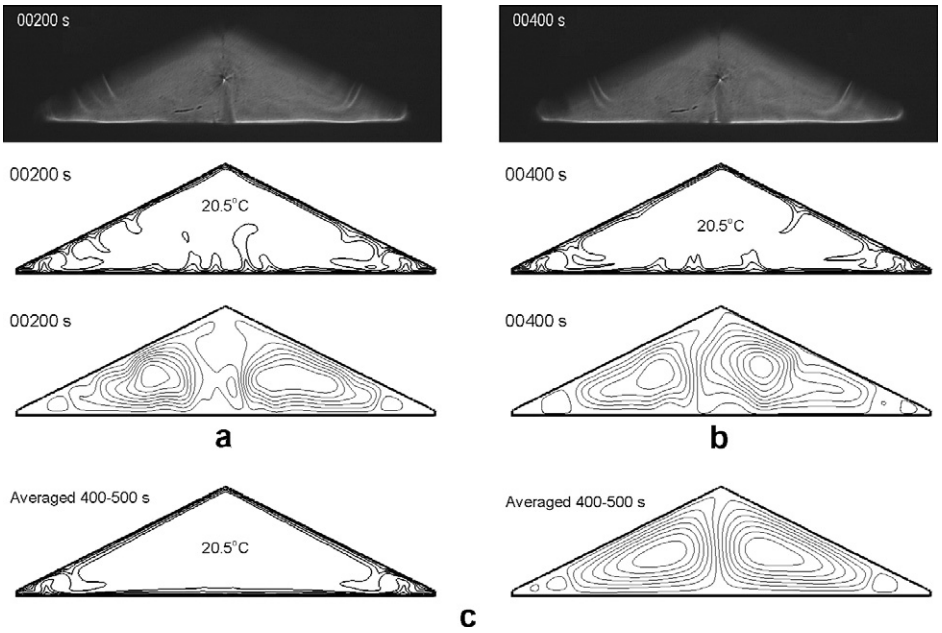

Fig. 5. Quasi-steady stage flow for $Gr = 2.36 \times 10^5$. From top to bottom: shadowgraph images, isotherms with 1 °C interval, and contours of stream functions with intervals of (a) 1.68×10^{-3} and (b) 2.0×10^{-3} m^2/s. (c) Time-averaged quasi-steady stage flow. (left) Isotherms with 1 °C interval; (right) contours of stream functions with an interval of 1.6×10^{-3} m^2/s.

4.1.3. Quasi-steady stage flow

Late in the transitional stage, a pitchfork bifurcation [4] starts to happen. As a consequence, an asymmetric flow structure is formed. It has been noted previously that the pitchfork bifurcation takes places at an earlier time in the experiment than that in the numerical simulation. An interesting phenomenon observed from both the experiment and the numerical simulation is that the convective instabilities occur alternatively on the left and right sides of the enclosure, and the horizontally traveling hot-water plumes from the two sides of the enclosure arrive at the center at alternative times. It is also observed in this study that the upwelling flow near the center of the enclosure oscillates about the geometric symmetry plane. However, it is expected that the time-averaged flow remains approximately symmetric about the geometric symmetry plane despite the asymmetry of the instantaneous flow.

The quasi-steady stage flow, which is shown in Fig. 5a and b for two different times, is characterized by the flow structure formed at the late transitional stage described above. The basic flow consists of gravity currents flowing downwards along the inclined surfaces and then turning horizontally toward the center of the enclosure along the base. At the center of the enclosure, the flow appears like a large rising thermal. As a consequence, the primary flow comprises two major convective cells, one on each side of the geometric symmetry plane (refer to the stream function contours in Fig. 5). At this stage, the convective instabilities described previously are still present, but are confined mainly in the regions near the two bottom tips and near the center of the enclosure (refer to the shadowgraph images and numerical isotherms in Fig. 5). The occurrence of the convective instabilities results in a number of small secondary convective cells in the enclosure. It is clear in Fig. 5a and b that the strength of the convective instability has decreased further from the previous stage. This flow structure remains as long as the present experiment and simulation lasted (about 900 s in the experiment and 1000 s in the simulation).

Fig. 5c plots the time-averaged flow at the quasi-steady state ($t = 400$ to 500 s) for $Gr = 2.36 \times 10^5$. Clearly, the time-averaged flow is approximately symmetric about the geometric symmetry plane. The slight asymmetry shown in Fig. 5c may be attributed to the finite number of data sets used to calculate the average flow.

4.2. Flow development and structures at different Grashof numbers

4.2.1. Experimental observations

As described in Section 2, five sets of flow visualization experiments are conducted in this study. These experiments are confined within a relatively narrow range of Grashof numbers, i.e. from 1.18×10^5 to 4.73×10^5. Within this Grashof number range, very similar features of the overall flow development are observed from the shadowgraph images. That is, the flow development can be classified into an early stage, a transitional stage and a quasi-steady stage, and the characteristics of the flow at each stage are similar for all Grashof numbers. Moreover, the instantaneous flow undergoes a transition from symmetry to asymmetry during the transitional stage. However, the experiments also indicate that the time-averaged flow at the quasi-steady

stage remains approximately symmetric irrespective of the Grashof numbers.

The present flow visualization has also demonstrated distinct variations of certain flow features at different Grashof numbers. On the one hand, the primary circulations become stronger as the Grashof number increases. On the other hand, the convective instabilities intensify with the Grashof number. As a consequence, more convective cells are formed in the transitional and quasi-steady stages at higher Grashof numbers. Moreover, the transition time from the start-up to the quasi-steady state is much shorter at higher Grashof numbers. This will be further discussed later based on the numerical data. The comparisons of the quasi-steady state flow structures observed for different Grashof numbers can be found in Fig. 6. It is seen in this figure that, at the quasi-steady state, the region affected by the convective instability expands as the Grashof number increases. At the lowest Grashof number ($Gr = 1.18 \times 10^5$), the convective instabilities are limited to very small regions near the tips (Fig. 6a). However, at the highest Grashof number ($Gr = 4.73 \times 10^5$), the convective instabilities are present almost everywhere in the enclosure (Fig. 6d).

4.2.2. Numerical observations

The present numerical simulations cover a much broader Grashof number range (5.91×10^3–4.73×10^5) compared to the experiments, and different features of the transient flows have been observed over the range of Grashof numbers. The overall flow development at different Grashof numbers can be seen in Fig. 7, which shows the time series of the average Nusselt numbers over the base of the enclosure. Here, the surface average Nusselt number $\overline{Nu}$ is defined as

$$\overline{Nu} = \frac{\bar{h}H}{k} = \frac{\bar{q}''H}{k\Delta T}. \tag{9}$$

At any position along the base, the local surface heat flux is calculated using Fourier's law as

$$q'' = -k\left.\frac{\partial T}{\partial y}\right|_{y=0}. \tag{10}$$

It is seen in Fig. 7 that the overall development of the transient flows can be roughly characterized by three stages, consistent with the previous flow visualizations based on the experiments and simulations. In the early stage, the surface Nusselt number decreases steadily until

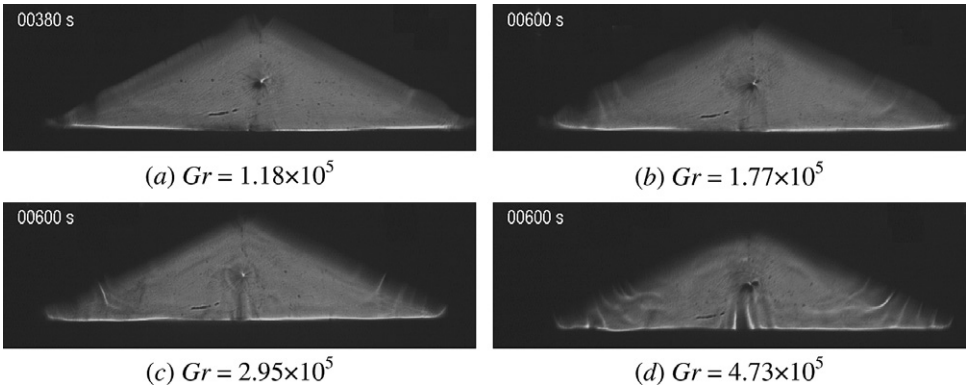

Fig. 6. Shadowgraphs of quasi-steady flow for different Grashof numbers.

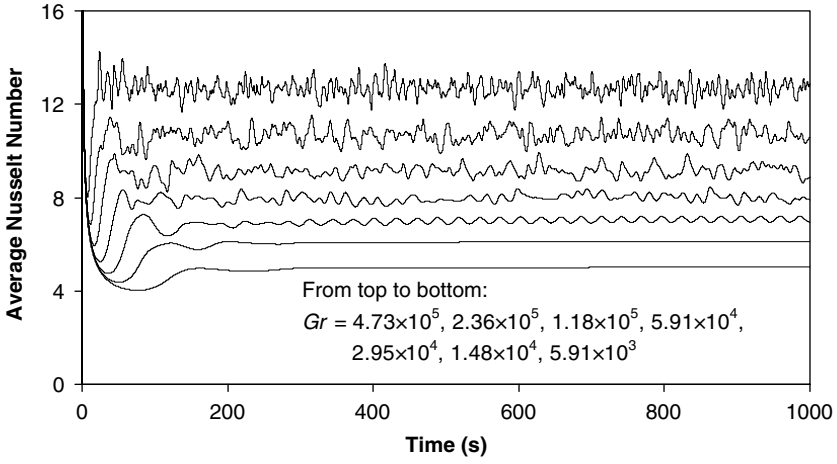

Fig. 7. Time histories of the average Nusselt numbers over the base for different Grashof numbers.

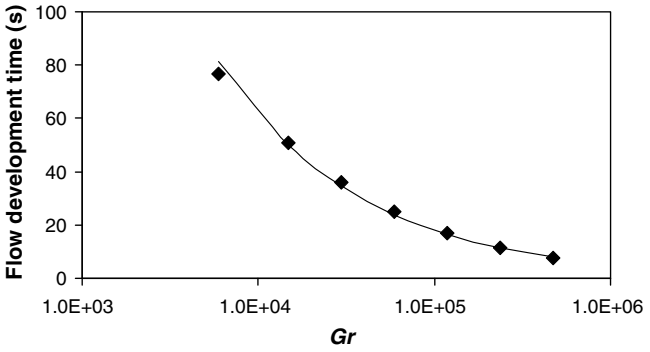

Fig. 8. Flow development time for different Grashof numbers.

the appearance of an undershoot, following which the transitional stage begins. The transitional stage flow is dominated by flow instabilities and wavy structures. After a certain period of time, the flow reaches a steady or quasi-steady stage, d epending on the Grashof number. For the two lowest Grashof number cases ($Gr = 5.91 \times 10^3$ and 1.48×10^4), the flow becomes steady after the transition, whereas for all other cases, the flow reaches a quasi-steady state after the transition. It is clear in Fig. 7 that the development of the flow is faster at higher Grashof numbers. While the time for reaching the steady or quasi-steady state is difficult to measure, the flow development time can be roughly indicated by the time of the appearance of the undershoot, which is plotted in Fig. 8. The filled diamonds in this figure represent the measured data from the simulations, and the solid line is a best-fit curve, which is given by

$$t_s = 8257.9 Gr^{-0.532} \quad \text{(s)}. \tag{11}$$

Fig. 9 shows the typical steady or quasi-steady state temperature and flow structures obtained for all the numerical

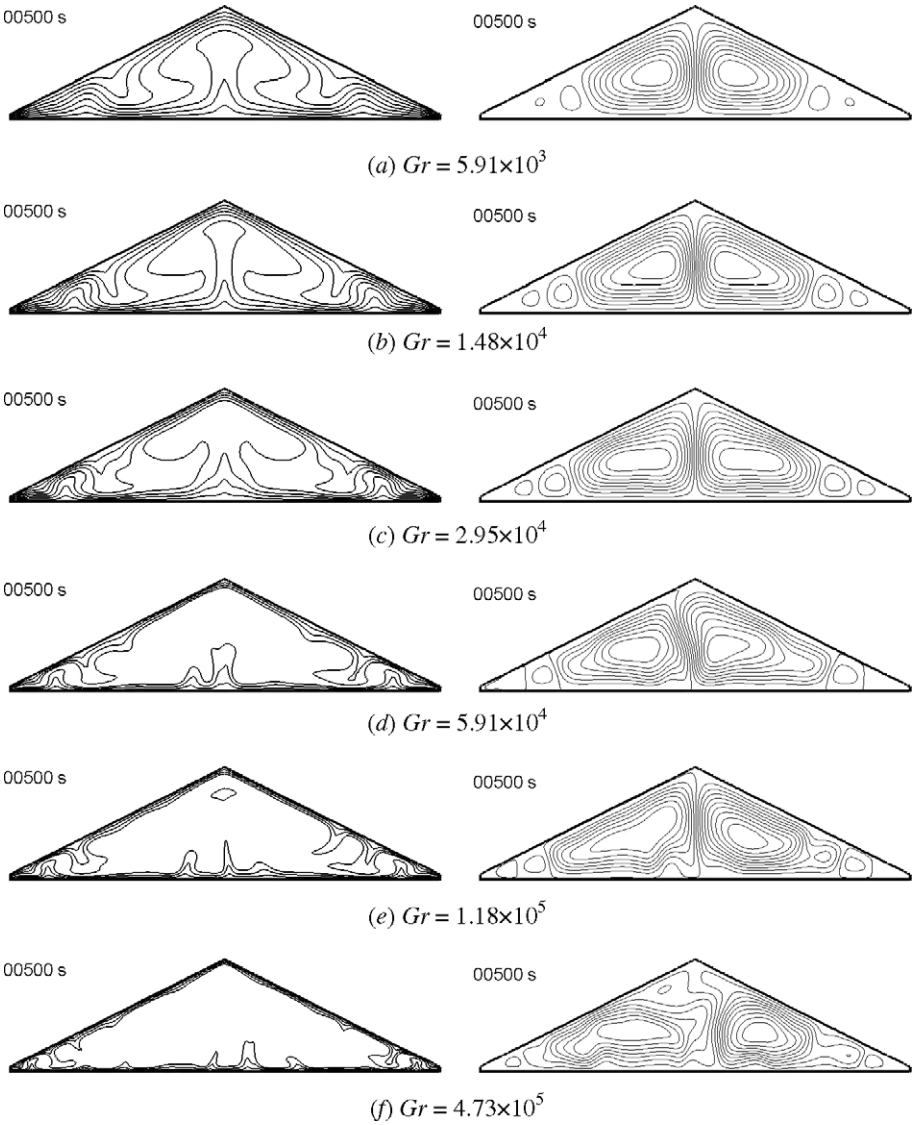

Fig. 9. Quasi-steady flow obtained numerically for different Grashof numbers. (left) Isotherms with intervals of (a) 0.025, (b) 0.0625, (c) 0.125, (d) 0.25, (e) 0.5 and (f) 2 °C. (right) Contours of stream functions with intervals of (a) 2.27×10^{-4}, (b) 3.58×10^{-4}, (c) 4.66×10^{-4}, (d) 7.19×10^{-4}, (e) 1.06×10^{-3} and (f) 2.12×10^{-3} m^2/s.

cases except case 6, which has been shown previously. Comparisons of the numerical results for the different Grashof numbers reveal certain variations of the flow features with the Grashof number. First, the primary circulations become stronger as the Grashof number increases, which can be seen from the contours of the stream functions in Fig. 9. Second, the numerical isotherms in this figure demonstrate that the convective instabilities are present even at the lowest Grashof number case, and the instabilities intensify, and the wave number associated with the convective instabilities increases with the Grashof number. Third, it is seen in Fig. 9 that, at the steady or quasi-steady state, the unstable region of the cooling thermal boundary layer expands from the lower tip regions toward the apex as the Grashof number increases.

Finally, Fig. 9 also reveals that the steady or quasi-steady state flow undergoes a transition from symmetric to asymmetric structures about the geometric symmetry plane as the Grashof number increases. It is seen in this figure that the steady flows at the Grashof numbers $Gr = 5.91 \times 10^3$ and 1.48×10^4 are symmetric. The quasi-steady flow at $Gr = 2.95 \times 10^4$ also appears to be symmetric. However, quantitative examinations of the temperature and flow fields (refer to Section 4.3) reveals that very weak asymmetry is developing in the flow at this Grashof number. For all other Grashof numbers above 2.95×10^4, the quasi-steady flows are clearly asymmetric. Therefore, the critical Grashof number for the transition from symmetric to asymmetric structures lies between $Gr = 1.48 \times 10^4$ and 2.95×10^4, and is expected to be very close to $Gr = 2.95 \times 10^4$.

The present critical Grashof number for the transition is about three times higher than that reported in [3] for air at the same aspect ratio (for $A = 0.5$, $Gr_c = 8930$). The variation may be attributed to the different fluid media, which have different Prandtl numbers. Furthermore, the structure of the asymmetric flow observed with air is also different from the present asymmetric flows with water. In the case with air as the medium, the mean flow at the steady state consists of a dominant circulating cell located at the center of the isosceles triangular enclosure, with additional smaller cells located on both sides of the dominant cell [3,4]. However, in the present case with water as the medium, the time-averaged flow remains approximately symmetric about the geometric symmetry plane (refer to Fig. 5c), despite the asymmetry of the instantaneous flows.

4.3. Observation of the pitchfork bifurcation

As discussed in [3,4], the transition of the flow from symmetry to asymmetry is due to the occurrence of a pitchfork bifurcation. The pitchfork bifurcation is observed in different ways in this section.

Fig. 10a shows two time series of the calculated temperatures at two locations within the heating thermal boundary layer for $Gr = 2.36 \times 10^5$. Here, T_2 is taken at the location $(-0.024, 0.001\text{ m})$, and T3 is taken at (0.024, 0.001 m). These two locations are symmetric about the geometric symmetry plane. It is seen in Fig. 10a that the two plots overlap for a significant period of time, indicating that the flow remains symmetric about the geometric symmetry plane during the period. The two temperature time series start to diverge at a time between 100 and 200 s, confirming the occurrence of the pitchfork bifurcation and the subsequent transition of the flow to asymmetry. The divergence of the two time series can be better viewed in Fig. 10b, which plots the time history of the temperature difference between these two locations.

It is expected that there is no flow exchange between the two sides of the enclosure along the geometric symmetry plane if the flow is symmetric. Therefore, the horizontal component of the velocity along the symmetry plane is zero in symmetric flows. When the pitchfork bifurcation occurs, the flow becomes asymmetric. There will be a net flow exchange between the two regions, and thus the horizontal component of the velocity will no longer be zero everywhere along the geometric symmetry plane. The time history of the maximum magnitude of the horizontal velocity component in the geometric symmetry plane for the same Grashof number as above is plotted in Fig. 10c, in which a zero value indicates a symmetric flow, and a non-zero value indicates an asymmetric flow. It is clear in Fig. 10c that the pitchfork bifurcation occurs at a time shortly after 100 s.

Associated with the asymmetric flow due to the pitchfork bifurcation, variations of the heat transfer between the left and right roofs are observed. This is seen in Fig. 10d and e, which plot the time histories of the surface average Nusselt numbers on the two inclined surfaces as well as the difference between them. The negative Nusselt numbers in Fig. 10d suggest that heat is transferred out of the enclosure through the inclined surfaces. Fig. 10d and e confirm the above-described features of the flow transition from symmetry to asymmetry associated with the pitchfork bifurcation. However, the indicated time for the occurrence of the pitchfork bifurcation in Fig. 10e is significantly behind that indicated in Fig. 10c. This is because the calculated Nusselt number represents an integrated feature over the surface, whereas the plotted quantity in Fig. 10c depends on the local flow, and thus is more sensitive to the pitchfork bifurcation than the Nusselt number. It is also worth noting that, despite the variation of the calculated heat fluxes and Nusselt numbers between the two inclined surfaces with the occurrence of the pitchfork bifurcation, no significant variation of the time-averaged heat fluxes and Nusselt numbers between the two inclined surfaces has been observed. Among the Grashof number range examined in this study, the maximum variation of these quantities between the two inclined surfaces is less than 2%.

From the results presented in Fig. 10, the critical time for the onset of the pitchfork bifurcation can be obtained. It is seen in Fig. 10 that the occurrence of the pitchfork bifurcation is clearly indicated by the time history plots

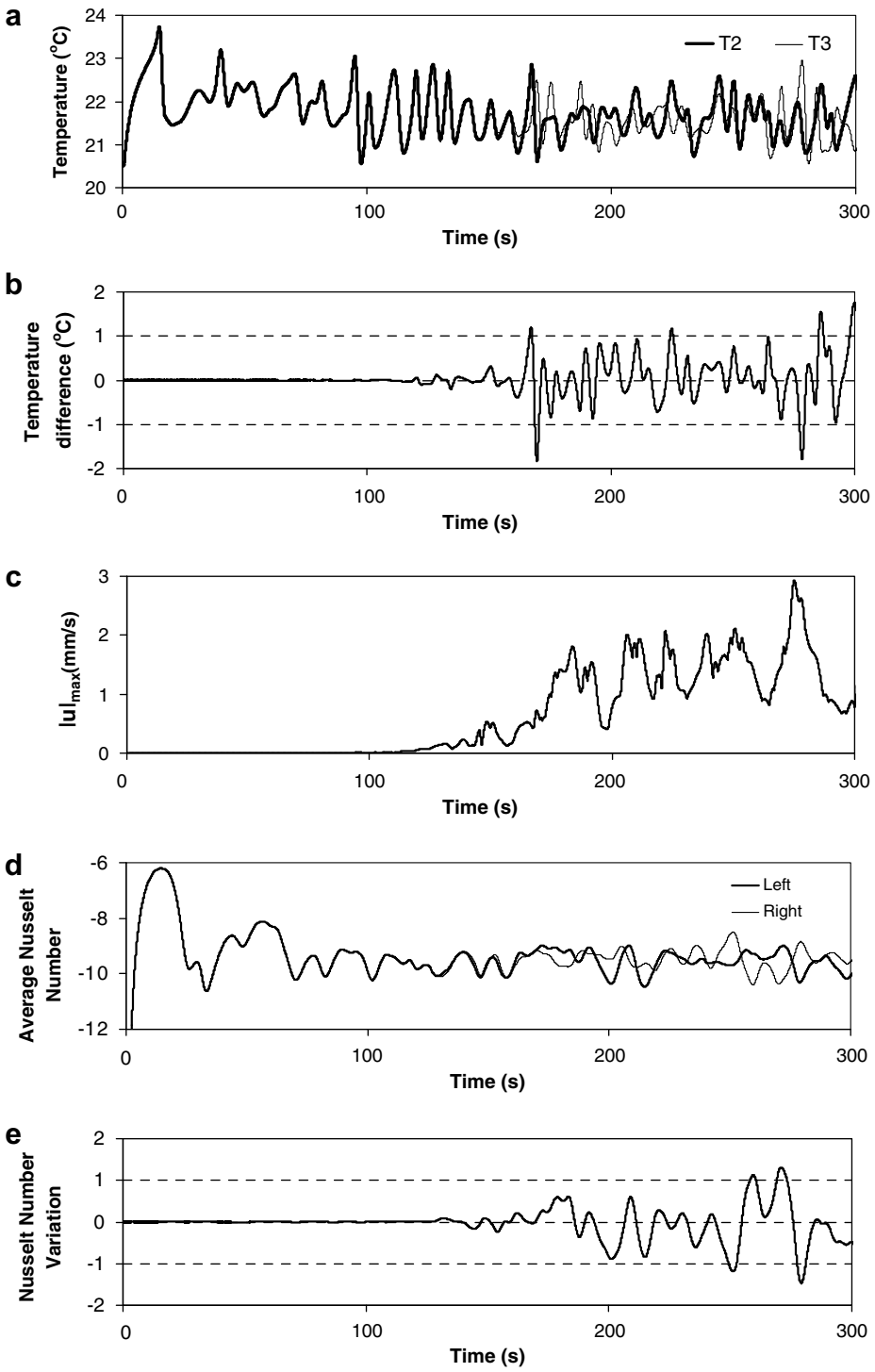

Fig. 10. Observation of the occurrence of the pitchfork bifurcation ($Gr = 2.36 \times 10^5$).

of the temperature difference between the two discrete locations (Fig. 10b), the maximum magnitude of the horizontal velocity component along the symmetry plane (Fig. 10c), and the variation of the Nusselt numbers between the left and right roofs (Fig. 10e). However, these three plots indicate different onset times for the same event, with the velocity plot (Fig. 10c) giving the earliest onset time, the Nusselt number plot (Fig. 10e) giving the latest onset time, and the temperature plot (Fig. 10b) giving an onset time between the other two. In this study, the onset time of the pitchfork bifurcation is determined based on the plot of the maximum magnitude of the horizontal velocity component in the geometric symmetry plane (Fig. 10c), which is the most sensitive to the pitchfork bifurcation. Since there is no definite criterion for determining the onset of the pitchfork bifurcation, it is approximately determined as the time

when the maximum magnitude of the horizontal velocity component along the symmetry plane (refer to Fig. 10c) first reaches one percent (1%) of its time-averaged value at the quasi-steady state. The obtained critical time for the transition at different Grashof numbers is plotted in Fig. 11, and it is scaled with the Grashof number according to the following relation:

$$t_c = 9.46 \times 10^4 Gr^{-0.564} \quad \text{(s)}. \tag{12}$$

4.4. Heat transfer rate

The flow visualization and quantitative results shown previously clearly indicate that natural convection in the isosceles triangular enclosure intensifies as the Grashof number increases. In particular, the convective instabilities are stronger at higher Grashof numbers. As a consequence, the heat transfer rate across the enclosure increases with the Grashof number. The heat transfer rate can be measured by the dimensionless Nusselt number. Fig. 12 plots the time-averaged Nusselt numbers over the base and inclined surfaces (roofs) for different Grashof numbers. Note that the Nusselt number at the base is greater than that at the inclined surfaces. This is because the base has a relatively smaller surface area for heat transfer. It is clear in Fig. 12 that the calculated Nusselt numbers increase with the Grashof number, indicating the increase of the heat transfer rate with the Grashof number. It is found from the present numerical simulations that the time-averaged

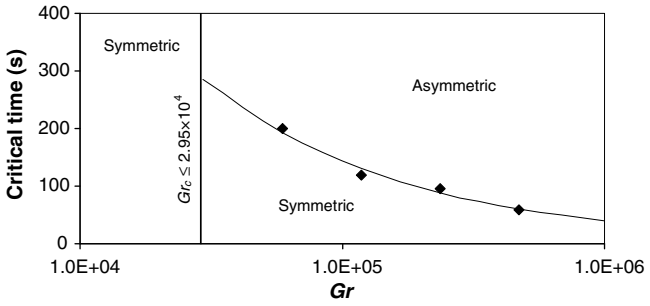

Fig. 11. Critical time for the occurrence of the pitchfork bifurcation.

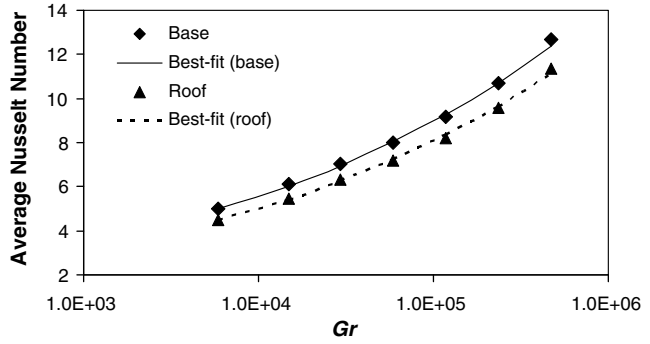

Fig. 12. Time-averaged Nusselt number over the base and roofs.

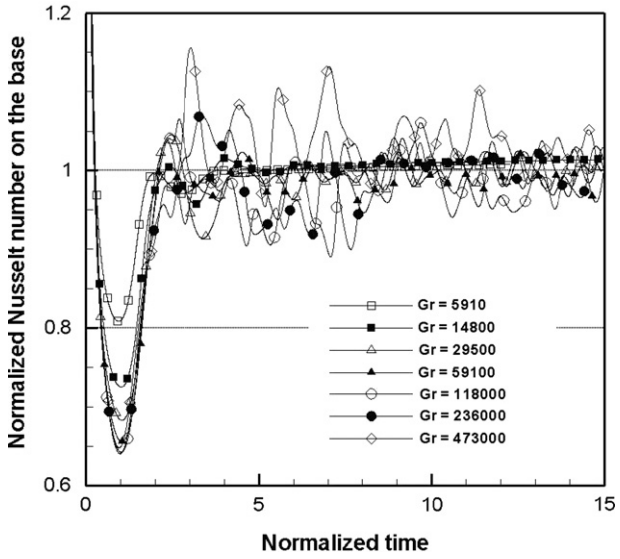

Fig. 13. Normalized time histories of the average Nusselt numbers over the base for different Grashof numbers.

Nusselt numbers over the base and roofs scale with the Grashof number according to the following relations:

$$|\overline{Nu}|_{\text{base}} = 0.826 Gr^{0.207}, \tag{13}$$

$$|\overline{Nu}|_{\text{roof}} = 0.743 Gr^{0.207}. \tag{14}$$

The time histories of the calculated average Nusselt number over the base for different Grashof numbers are re-plotted in Fig. 13. Here, the time is normalized with the flow development time t_s given by Eq. (11), and the Nusselt number is normalized with the time-averaged Nusselt number $|\overline{Nu}|_{\text{base}}$ given by Eq. (13). It is seen in Fig. 13 that the undershoots at the early stage for different Grashof numbers are aligned at the non-dimensional time of 1, and the normalized Nusselt number at the steady/quasi-steady state approaches to a mean value of 1 for all Grashof numbers. These plots confirm the correctness of the relevant time and Nusselt number scales obtained previously from the present numerical simulations.

5. Conclusion

In this study, the natural convection flow in an isosceles triangular enclosure subject to abrupt heating from the base and simultaneous cooling from the inclined surfaces is investigated both experimentally and numerically. The flow is visualized using a shadowgraph technique, and simulated using a Finite Volume Method for a fixed aspect ratio $A = 0.5$ and a range of Grashof numbers from 5.91×10^3 to 4.73×10^5. Both the experiments and numerical simulations have revealed that the transient flow development in the enclosure following the startup can be classified into three distinct stages, an early stage, a transitional stage, and a steady/quasi-steady stage. The early stage flow is characterized by the growth of thermal boundary layers adjacent to all the interior surfaces and the

initiation of primary circulations. The transitional stage flow is characterized by the appearance of convective instabilities in the form of rising and sinking thermals and the formation of cellular flow structures. The steady-state flow at low Grashof numbers is characterized by symmetric flows about the geometric symmetry plane, and the quasi-steady flow at relatively higher Grashof numbers is characterized by the pitchfork bifurcation, which results in alternative occurrence of convective instabilities from the two sides of the enclosure and the oscillation of the upwelling flow near the center.

Furthermore, the present study has provided a time scale for the development of the flow in the enclosure (Eq. (11)). This time scale in fact approximately represents the time for the onset of convective instabilities.

The transition of the flow from symmetry to asymmetry due to the pitchfork bifurcation has been examined in detail in this study, and a critical Grashof number close to $Gr = 2.95 \times 10^4$ has been identified for the present aspect ratio ($A = 0.5$). The discrepancy of the critical Grashof number obtained here with that reported in [3] may be attributed to the different fluid media in these two studies. A critical time, given by Eq. (12), has also been obtained for the onset of the pitchfork bifurcation. It is worth noting that, an approximately symmetric time-averaged flow is retained at the quasi-steady stage for all the high Grashof numbers considered in this study despite the asymmetry of the instantaneous flows in the enclosure. This flow feature is clearly different from the steady symmetric flow reported in [3].

Finally, the features of the heat transfer through the enclosure have been examined based on the numerical simulations. The present investigation has produced scales (Eqs. (13) and (14)) for estimating the time-averaged Nusselt numbers across the base and inclined surfaces.

Acknowledgements

This research was financially supported by James Cook University and the Australian Research Council.

References

[1] D. Poulikakos, A. Bejan, Natural convection experiments in a triangular enclosure, J. Heat Transfer, Trans. ASME 105 (1983) 652–655.
[2] D. Poulikakos, A. Bejan, The fluid dynamics of an attic space, J. Fluid Mech. 131 (1983) 251–269.
[3] G.A. Holtzman, R.W. Hill, K.S. Ball, Laminar natural convection in isosceles triangular enclosures heated from below and symmetrically cooled from above, J. Heat Transfer, Trans. ASME 122 (2000) 485–491.
[4] E.H. Ridouane, A. Campo, Formation of a pitchfork bifurcation in thermal convection flow inside an isosceles triangular cavity, Phys. Fluids 18 (2006) 074102.
[5] R.D. Flack, T.T. Konopnicki, J.H. Rooke, The measurement of natural convective heat transfer in triangular enclosures, J. Heat Transfer, Trans. ASME 101 (4) (1979) 648–654.
[6] V.A. Akinsete, T.A. Coleman, Heat transfer by steady laminar free convection in triangular enclosures, Int. J. Heat Mass Transfer 25 (7) (1982) 991–998.
[7] E.M.d. Campo, M. Sen, E. Ramos, Analysis of laminar natural convection in a triangular enclosure, Numer. Heat Transfer 13 (1988) 353–372.
[8] H. Salmun, Convection patterns in a triangular domain, Int. J. Heat Mass Transfer 38 (2) (1995) 351–362.
[9] H. Asan, L. Namli, Laminar natural convection in a pitched roof of triangular cross-section: summer day boundary conditions, Energy Build. 33 (2000) 69–73.
[10] H. Asan, L. Namli, Numerical simulation of buoyant flow in a roof of triangular cross-section under winter day boundary conditions, Energy Build. 33 (7) (2001) 753–757.
[11] S.C. Tzeng, J.H. Liou, R.Y. Jou, Numerical simulation-aided parametric analysis of natural convection in a roof of triangular enclosures, Heat Transfer Eng. 26 (8) (2005) 69–79.
[12] E.H. Ridouane, A. Campo, M. McGarry, Numerical computation of buoyant airflows confined to attic spaces under opposing hot and cold wall conditions, Int. J. Therm. Sci. 44 (10) (2005) 944–952.
[13] E.H. Ridouane, A. Campo, M. Hasnaoui, Benefits derivable from connecting the bottom and top walls of attic enclosures with insulated vertical side walls, Numer. Heat Transfer A: Appl. 49 (2006) 175–193.
[14] E.H. Ridouane, A. Campo, M. Hasnaoui, Turbulent natural convection in an air-filled isosceles triangular enclosure, Int. J. Heat Fluid Flow 27 (3) (2006) 476–489.
[15] H.F. Oztop, Y. Varol, A. Koca, Laminar natural convection heat transfer in a shed roof with or without eave for summer season, Appl. Therm. Eng. 27 (2007) 2252–2265.
[16] A. Koca, H.F. Oztop, Y. varol, The effects of Prandtl number on natural convection in triangular enclosures with localized heating from below, Int. Commun. Heat Mass Transfer 34 (2007) 511–518.
[17] R.D. Flack, The experimental measurement of natural convection heat transfer in triangular enclosures heated or cooled from below, J. Heat Transfer, Trans. ASME 102 (1980) 770–772.
[18] Y.E. Karyakin, Y.A. Sokovishin, O.G. Martynenko, Transient natural convection in triangular enclosures, Int. J. Heat Mass Transfer 31 (9) (1988) 1759–1766.
[19] C. Lei, F. Xu, J.C. Patterson, Visualisation of natural convection in an isosceles triangular enclosure heated from below, in: B.E. Milton (Ed.), Proceedings of the Fifth Pacific Symposium on Flow Visualisation & Image Processing(CD-ROM), 2005, Paper No. PSFVIP-5-229.
[20] P.M. Haese, M.D. Teubner, Heat exchange in an attic space, Int. J. Heat Mass Transfer 45 (2002) 4925–4936.
[21] W. Merzkirch, Flow Visualisation, Academic Press, New York, 1974.
[22] G.S. Settles, Schlieren and Shadowgraph Techniques, Springer, Heidelberg, 2001.
[23] W. Schöpf, J.C. Patterson, Natural convection in a side-heated cavity: visualization of the initial flow features, J. Fluid Mech. 295 (1995) 279–357.
[24] W. Schöpf, J.C. Patterson, Visualization of natural convection in a side-heated cavity: transition to the final steady state, Int. J. Heat Mass Transfer 39 (1996) 3497–3509.
[25] C. Lei, J.C. Patterson, Natural convection in a reservoir sidearm subject to solar radiation: experimental observations, Exp. Fluids 32 (5) (2002) 590–599.
[26] F. Xu, J.C. Patterson, C. Lei, Shadowgraph observations of the transition of the thermal boundary layer in a side-heated cavity, Exp. Fluids 38 (6) (2005) 770–779.
[27] F. Xu, J.C. Patterson, C. Lei, Experimental observations of the thermal flow around a square obstruction on a vertical wall in a side-heated cavity, Exp. Fluids 40 (3) (2006) 364–371.
[28] S.V. Patankar, Numerical Heat Transfer and Fluid Flow, Hemisphere Publishing Corporation, 1980.
[29] J.C. Patterson, S.W. Armfield, Transient features of natural convection in a cavity, J. Fluid Mech. 219 (1990) 469–497.